Energy 252 (2022) 124008

Contents lists available at ScienceDirect

Energy

journal homepage: www.elsevier.com/locate/energy

The effect of syngas addition on flameless natural gas combustion in a regenerative furnace

Hernando A. Yepes [a], Julián E. Obando [b], Andrés A. Amell [b, *]

[a] Grupo de Investigación en Nuevas Tecnologías, Sostenibilidad e Innovación, GINSTI, Departamento de Ingeniería Mecánica, Universidad Francisco de Paula Santander Ocaña, Ocaña, Colombia
[b] Grupo de Ciencia y Tecnología Del Gas y Uso Racional de La Energía GASURE, Facultad de Ingeniería, Universidad de Antioquia, Medellín, Colombia

ARTICLE INFO

Article history:
Received 8 July 2021
Received in revised form
30 March 2022
Accepted 11 April 2022
Available online 14 April 2022

Keywords:
Flameless
Syngas
Regenerative furnace
Hydrogen

ABSTRACT

The present work numerically and experimentally studies the mixture of 30% syngas and 70% natural gas (SG-NG), by volume, and compares performance to pure natural gas (NG). The experimental measurements were carried out in a semi-industrial regenerative furnace originally designed for pure natural gas. A 25 kW thermal input and a 1.2 excess air ratio were maintained throughout. Temperatures and species were measured inside the combustion chamber. The effect of the syngas on the reaction zone location was determined by imaging spontaneous chemiluminescence. The effect of preheating was also studied for the SG-NG mixture. CFD modeling was used to analyze the effects on recirculation patterns. SG-NG exhibited an average temperature decrease of 6% compared to NG, due to the greater recirculation and increased CO_2 in the flue gases. The species uniformity remained consistent, while the thermal uniformity factor (RTU) decreased by 10.5%, indicating greater uniformity. NOx emissions decreased by almost 50% for the SG-NG mixture. The addition of syngas improved the reactivity and displaced the reaction zone upstream. Without preheating, the recirculation and the reactant dilution decrease, generating a disturbance in the thermal uniformity (RTU increase by 65%) and the reaction zone was displaced downstream.

© 2022 The Authors. Published by Elsevier Ltd. This is an open access article under the CC BY-NC-ND license (http://creativecommons.org/licenses/by-nc-nd/4.0/).

1. Introduction

H_2-enriched fuels, such as syngas, are an excellent alternative energy step towards reduced fossil fuel dependence and pollutant emissions. The high reactivity of the H_2 in a syngas mixture leads to greater reaction rates and improved combustion, reducing emissions from incomplete combustion [1,2]. However, implementing these fuels in conventional burners encounters various issues. The greater combustion temperature of H_2 may damage some burner elements and stimulate pollutant formation, such as NOx via the thermal route. Furthermore, compared to conventional fuels, the resulting combustion properties can produce undesired phenomena like flashback or early autoignition [3,4].

Flameless combustion presents a great technique for taking advantage of H_2-enriched fuels. The above mentioned issues are mitigated by the distributed nature of flameless combustion, i.e. the high dilution of the reactants with flue gases before the reaction process occurs [5,6]. Lacking a concentrated combustion zone and flame, flashback does not occur, while the reduced temperatures prevent autoignition and burner component damage. However, there are certain drawbacks when a conventional fuel is partially or totally replaced by syngas in a flameless combustion system. Changes in the low heating value and the stoichiometric air mass can produce critical disturbances in the recirculation flow due to momentum flux variations in the reactant discharge jets. The increased fuel mass flow, in order to conserve the thermal input, may lead to excessive recirculation, causing a drastic drop in the reaction rates and increased emissions by incomplete combustion. On the other hand, lower dilution can result in conventional flames and high temperatures zones, promoting NOx formation [7,8].

Contrary to the fossil fuels where large-scale and multi-burner experiments have been conducted [9–11], the research using H_2-enriched fuels at these scales is scarcer. Although several studies of H_2-enriched fuels have been carried out, many of them used experimental setups where recirculation and chemical interactions were decoupled, as is the case for jet-hot-coflow burners, opposite

* Corresponding author. Grupo de Ciencia y Tecnología del Gas y Uso Racional de la Energía GASURE, Facultad de Ingeniería, Universidad de Antioquia, Medellín, Colombia.
E-mail address: andres.amell@udea.edu.co (A.A. Amell).

https://doi.org/10.1016/j.energy.2022.124008
0360-5442/© 2022 The Authors. Published by Elsevier Ltd. This is an open access article under the CC BY-NC-ND license (http://creativecommons.org/licenses/by-nc-nd/4.0/).

burner flames, or perfectly stirred reactors [12–21]. Research where the kinetics and fluid dynamics are coupled, such as in furnaces or boiler burners, is more common for flameless fossil fuel combustion [22–34] as compared to H_2-hydrocarbon fuel mixtures [35–41] and in some cases only apply a numerical approach [42,43]. Few works study syngas in various practical devices [44–51]. Indeed, five of the eight referenced studies were performed in the same experimental combustor. Moreover, the present authors did not find any literature on flameless syngas/fossil fuel mixture combustion.

In various of the works studying H_2 and syngas fuels under flameless combustion conditions, certain real industrial processes are emulated and consequently move off from "real-life" scenarios [52]. For example, preheating the oxidizer artificially is common practice in flameless combustion research, while using heat recovery for preheating is an essential practice for adequate energy efficiency and can modify the aerodynamics inside the combustion chamber. Fortunato et al. [44] carried out a study using coke-oven gas (>60% H_2 by vol.) in a furnace at 30 kW to validate a reduced NO-formation mechanism, where the oxidizer was preheated by an electrical heater. Ayoub et al. [39] also electrically preheated the oxidizer to 858 K in their study. However, this temperature may not be obtained by a real heat recovery process and most likely would not be constant, depending instead on H_2 content and excess air ratio variations. Chinnici et al. [41,46,53] did not utilize exhaust gas energy recovery, although the combustor was equipped to do so. The trend is the same for studies with syngas. The burner used by Shabanian et al. [47] had a zone surrounded by an electrical heater to emulate the performance of a recuperative industrial heat exchanger. According to the experimental setup descriptions, the studies of Huang et al. [45,49–51] also did not have a preheating system coupled to the combustor, even though one of the works focused on the effect of air temperature, indicating that they used an external heater. However, in industrial systems, flameless combustion is achieved by internal recirculation, producing strong turbulence-chemistry interactions, which are difficult to model numerically or replicate by emulation. Therefore, more data of processes as close as possible to industrial conditions are needed to in order to optimize the models.

In certain cases, when the addition of a fuel changes the LHV, it is necessary to modify the nozzle diameter in order to maintain the recirculation level and maintain the flameless combustion regime. Huang et al. [45] used fuel nozzle diameters of 1.8 and 2.5 mm for LHVs of around 10 and 5 MJ/Nm^3, respectively. Colorado et al. [54] changed the diameter from 3.2 to 5 mm when the natural gas was replaced with biogas, changing the LHV from 9.43 to 5.66 kWh/m^{3}std, respectively.

Considering the above, the present study evaluates the effect of the addition of syngas (40% H_2, 40% CO, and 20% CO_2, by vol.) to natural gas in a semi-industrial furnace under flameless combustion conditions. The furnace was equipped with a regenerative system using heat recovered from flue gases to preheat the oxidizer, similar to industrial processes. The furnace also had a counter-flow heat exchanger to simulate a thermal load. The experiments were carried out at a thermal input of 25 kW and excess air ratio of 1.2. The species, temperatures, and reaction zones resulting from syngas-natural gas (SG-NG) mixture combustion were compared with those of pure natural gas (NG) combustion. Furthermore, the preheating and outflow of flue gas through the regenerators effects were also studied for the SG-NG case. Finally, a CFD model was used to determine the effects on recirculation patterns.

2. Experimental methodology

2.1. Experimental setup

A semi-industrial furnace with a regenerative burner developed by the GASURE group, initially designed to operate with natural gas, was used to carry out the experimental measurements. The burner nozzles were not modified when syngas was added to the fuel. The inlet and outlet flow schematics are shown in Fig. 1. The most relevant aspects of the furnace are presented below, while further details can be found in Refs. [54–56]. The combustion chamber has a square cross-section of 0.36 m^2 and a length of 1.35 m. The combustion chamber is surrounded by ceramic fiber with a thermal conductivity of 0.32 W/m-k to reduce heat losses. During the flameless mode, the oxidizer is discharged at high velocity by two of the peripheral nozzles, while the other two nozzles extract the

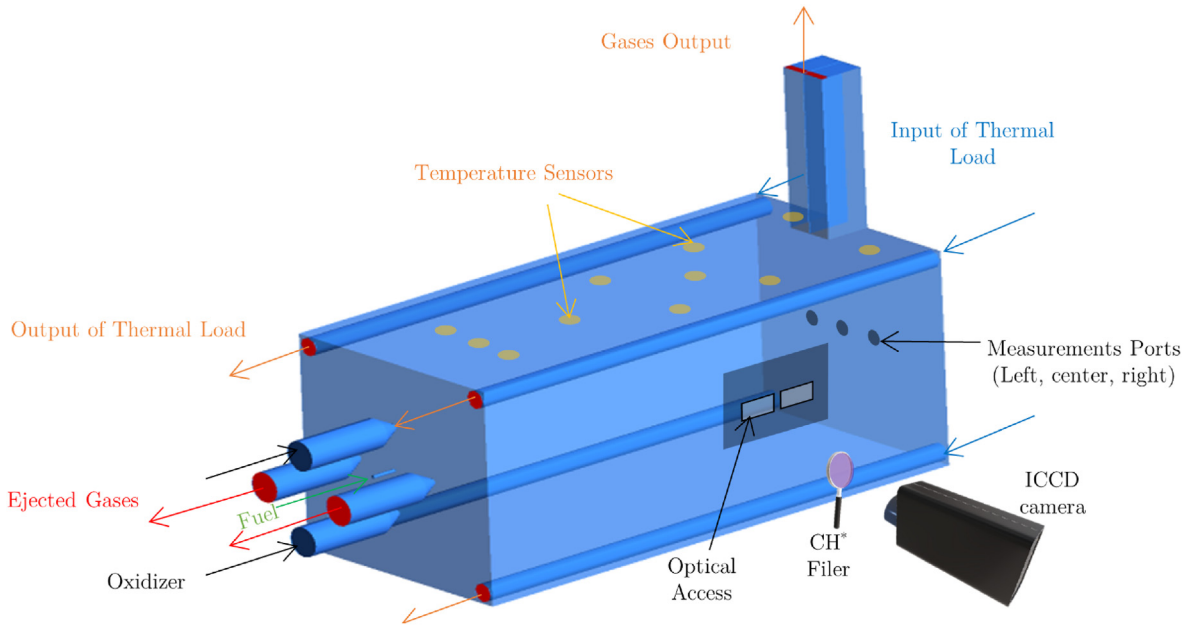

Fig. 1. Furnace schematic.

flue gases to the cordierite honeycomb regenerators, where part of the sensible heat is recovered to preheat the oxidizer.

Four steel tubes containing air flows run along the corners of the chamber to emulate a thermal load. The combustion chamber has two quartz glass windows in a lateral wall for monitoring the regime's stability, verifying the absence of visible flames, and imaging the reaction zone. At the end wall, three measurement ports separated by 15 cm along the central plane allow for the insertion of temperature and species sample probes. Thus, three measurements lines were established: left, center and right, the latter being nearest to the windows. Additionally, 11 fixed thermocouples are placed along the upper wall to characterize the thermal fields.

Fig. 2 presents the schematics of the temperature and species sample probes. The temperature sample probe is a suction pyrometer measuring 1.8 m, containing a type K thermocouple with a ceramic cover on the wire placed inside two concentric tubes that serve as protective shields in order to reduce the influence of radiation on the measurement [57,58]. The average uncertainty of the temperature (ΔT) for all experimental conditions with this sample probe was ±5 K. A cooled species sample probe was used in order to stop the reaction of the collected gases.

A SICH MAIHAK SS710 gas analyzer, coupled with a conditioning unit to remove steam, was used to measure CH_4 (0–100%), CO_2 (0–100%), CO (0–60.000 ppm), and O_2 (0–100%) species, on a dry basis. NO_x (0–100 ppm) emissions were measured using chemiluminescence with a Thermo-Scientific 42i analyzer. Hotwire meters were used to measure oxidizer and thermal-load airflows. The fuel flows were measured using specifically calibrated rotameters for each component with an uncertainty of 2e-5 kg/s (syngas and natural gas). The reaction zone was observed by capturing images of the spontaneous chemiluminescence with a Princeton Instruments PI-MAX ICCD camera. A band-pass filter restricted sensitivity to a wavelength range of 387 nm–430 nm, corresponding to the emissions of radicals relevant for hydrocarbon flames and flameless combustion, such as CH (390, 430 nm), CH_2O (395, 423 nm), and HCO (300–400 nm) [59–64].

The temperature and emissions contours are shown in section 4 obtained from experimental results are only indicative and with the idea of improving the visualization of the results trend. The specific data point is indicated explicitly in the figures. The color contours were calculated using an interpolation function in MATLAB from the experimental data.

2.2. Fuel composition and operating conditions

Pure NG and a SG-NG mixture were used as fuels for the experimental evaluation. The NG composition was approximated to 100% CH_4 for analytical proposes. Although this varies according to the extraction site, the principal component is the mentioned species [24,55,65,66]. The composition of the SG used was 40% H_2, 40% CO, and 20% CO_2, by vol., which corresponds approximately to syngas obtained from biomass gasification [67–69] and coal gasification by mean of Conoco/Phillips technology [70,71]. Finally, the SG-NG fuel mixture was 30% SG and 70% NG. Table 1 presents the compositions, low heating value, air mass ratio ($M_{a,\ stq}$), and CO_2 mass production at stoichiometric conditions for each fuel.

The operating conditions for the experiments are listed in Table 2. The air-fuel ratio, thermal input and load mass flow were maintained constant for NG and SG-NG fuels in order to compare the effect of syngas addition on the nominal operative conditions of the furnace. For the NG and SG-NG fuels, the regeneration system used to preheat (PH) the oxidizer was operated in cycles of 40 s.

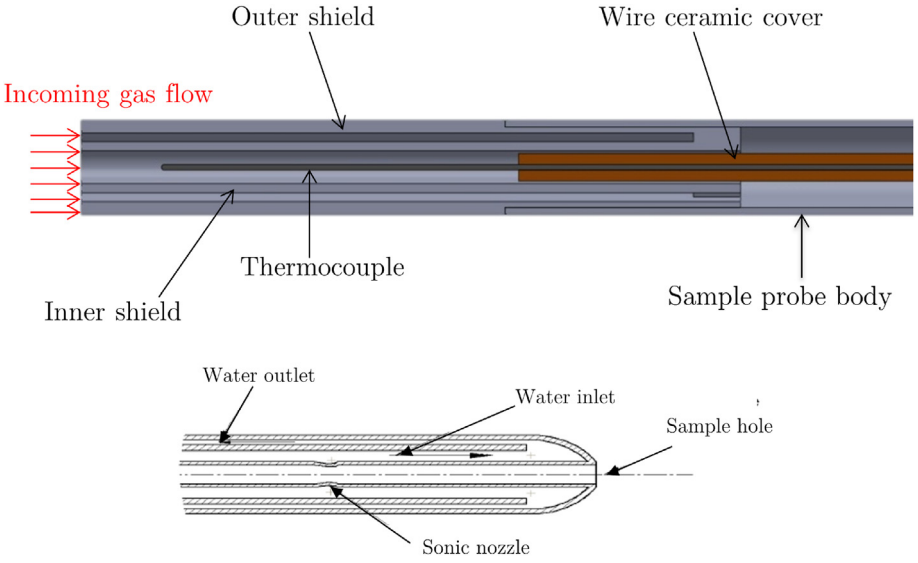

Fig. 2. Sample probes. Temperature (upper). Species (lower).

Table 1
Fuel compositions and properties.

	Natural gas (NG)	Syngas – Natural gas (SG-NG)
Compositions	100% CH_4	70% CH_4 12% H_2 12% CO 6% CO_2
LHV (Kw-h/kg)	13.89	9.93
LHV (kW-h/m^3_{std})	9.43	7.38
$M_{a,\ stq}$ (kg_{air}/kg_{fuel})	17.19	11.99
m_{CO2} (kg_{CO2}/kW)	0.197	0.222
Wobbe index (kW-h/m^3_{std})	12.68	10.48

Table 2
Experimental operating conditions.

	NG	SG-NG (PH)	SG-NG (WPH)
Fuel mass flow (kg/h) - $\dot{m}_f$	1.78	2.44	
Oxidizer mass flow (kg/h) - $\dot{m}_o$	36.75	35.47	
Air-fuel ratio	1.2		
Thermal input (kW)	25		
Load mass flow (kg/h)	136.11		
Heat flux to load tubes (kW/m^2)	54.8	51.9	44.1

This timing was fixed in order to achieve the high efficiency of the regenerators [72]. An additional test was performed without preheating (WPH) air and therefore, the switching and outflow of flue gas through the regenerators systems were disabled.

2.3. Thermal uniformity factor (RTU)

Thermal uniformity factor (RTU) was determined according to equation (1) [73]. This factor measures the uniformity of temperature fields inside the furnace and was used to quantify the thermal uniformity, which is one of the most relevant characteristics of flameless combustion.

$$RTU = \sqrt{\sum \left(\frac{T_i - \overline{T}}{\overline{T}}\right)^2} \quad (1)$$

2.4. Flameless combustion evaluation

The achievement of the flameless combustion regime was evaluated experimentally using the O_2 concentration, the temperature profile inside the combustion chamber, the visual inspection through optical access and the modified diagram combustion of Cavaliere and Joannon [6,74,75]. At flameless combustion conditions, the O_2 concentration, in general, should be lower than 15% (by volume) [54], although it depends on the type of fuel and oxidizer temperature. For CH_4 and mixtures with H_2, the value can decrease to 9.5% and 7.5%, respectively [20]. In the case of the present experiments, the O2 concentrations inside the combustion chamber were lower than these values, with an average value of around 4.3% for all cases. The contours and values are presented in the supplementary material. The temperature profiles are more uniform and flatter in the flameless combustion regime than conventional combustion. As is exposed in the result section, the RTU values and the temperature profiles of all cases are according to flameless combustion conditions.

No visible flames were observed in the visual inspection through the optical access of the furnace for all cases. Fig. 3 shows an image of the combustion chamber interior from the optical access for SG-NG(WPH), where due to the lower temperature, the apparition of conventional flames is most probably. As can be seen, no flames are present. For the other cases, similar images were observed.

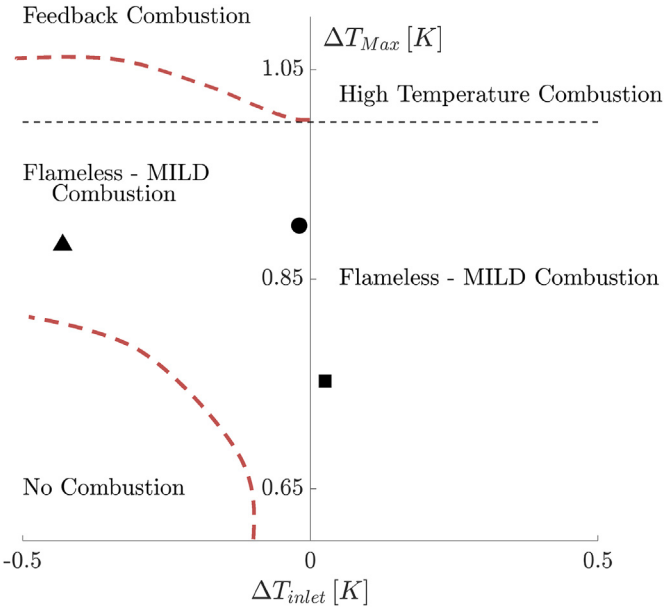

Fig. 4. Classification in a modified Cavaliere - Joannon diagram. Circle: NG. Square: SG-NG (PH). Triangle: SG-NG(WPH).

Finally, the modified diagram combustion of Cavaliere and Joannon was used to classify and verify the flameless combustion regime. ΔT_{max} and ΔT_{inlet} are defined according to equation (2) and(3). T_i, T_{ai}, and T_{max} are the inlet reagents temperature, the mixture's autoignition temperature, and the maximum temperature obtained in the furnace, respectively.

$$\Delta T_{max} = \frac{T_{max} - T_{in}}{T_{ai}} \quad (2)$$

$$\Delta T_{inlet} = \frac{T_{in} - T_{ai}}{T_{ai}} \quad (3)$$

Experimental measurements were used for the calculations. Fig. 4 shows the results for all cases. The red dashed lines are the approximate limits defined by Joannon et al. [75] for CH_4.

All cases classify as flameless combustion. Solely for SG-NG(PH),

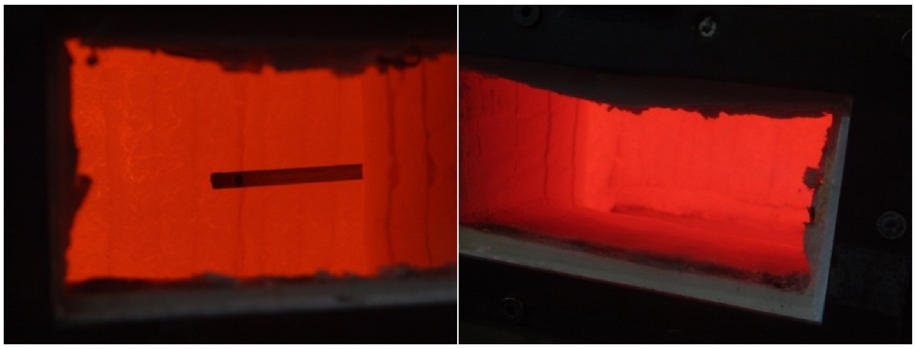

Fig. 3. Visual inspection inside the combustion chamber for SG-NG (WHP).

ΔT_{inlet} is positive and accomplishes the classical requirements for flameless conditions defined by Cavaliere and Joannon ($\Delta T_{max} <$ Tai and $\Delta T_{inlet} >0$) [6]. NG and especially SG-NG(WPH) are located in the Quasi-Mild region defined by Wang et al. [74]. However, all characteristics related to thermal profiles and emissions of the flameless regime are maintained in this region. The difference is that the combustion is not fully autoignited, since $T_i < T_{ai}$; although the temperature of the reactants is not high enough to ignite the mixture, the accumulation of the input heat energy carried by the oxidizer and the heat released by exothermic reactions can sustain slow combustion reactions.

3. Numerical methodology

A simulation using Ansys-Fluent 17.0 was carried out to analyze the effect of preheating air on flameless SG-NG combustion. Due to the symmetry of the furnace, only half of the combustion chamber was selected as the computational domain, using a hexahedral mesh of 405,632 cells. Fig. 5 shows the symmetric computational mesh. The simulations were performed at steady state, using the experimental operating conditions.

3.1. Physical and oxidation models

Three versions of the k-ε model were evaluated (standard, realizable, and RNG) using standard wall functions to solve for the viscous turbulent flow. Some authors have reported adequate results from these models for flameless combustion [17,24,42,44,65,76,77], motivating the present selection. The Discrete Ordinate model was used to solve the radiative transfer equation, while the weighted sum of gray gases (WSGG) model was implemented to calculate the absorption coefficient. The WSGG model used in the simulation is the default version of Ansys-Fluent; due to the simulation temperatures being between 600 and 2400 K, therefore the coefficients correspond to Smith et al. [78]. The Eddy Dissipation Concept model was selected for the reaction process due to the characteristically comparable physical and chemical times of flameless combustion, for which conventional fast chemistry models are not suitable. The five-step global reaction mechanism proposed for flameless combustion by Wang et al. [79] was used in the simulations. Boundary conditions are exposed in Table 3.

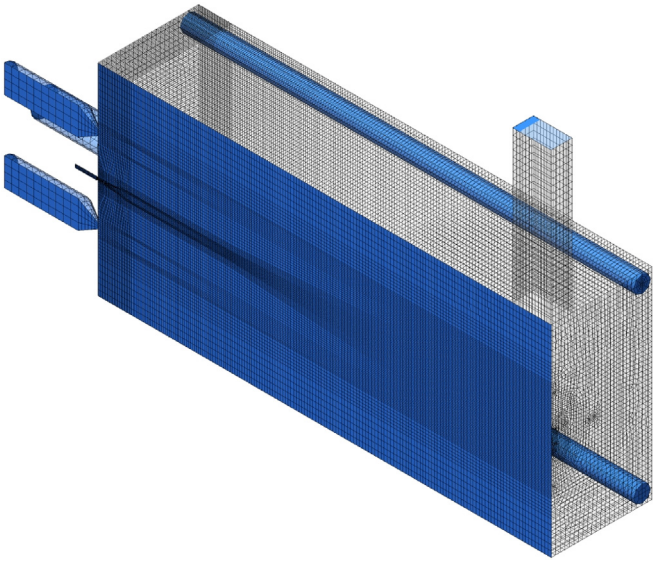

Fig. 5. Computational mesh for the combustion chamber 405,632 cells.

3.2. Numerical scheme and convergence criteria

A first-order discretization scheme was used to find the preliminary solution for the transport equations, subsequently applying the results as an initial guess for the second-order solution, taken as the final result. An independence mesh test was performed with two additional meshes of 840,521 and 1,191,921 cells. The temperature and velocity profiles along the center line were compared and no relevant differences were found. Additionally, the grid convergence index (GCI) proposed by Roache [80] was used to evaluate the discretization error and estimate the deviation of the final calculation from the asymptotic solution. The mesh independence and GCI data are included in the supplementary material. Convergence was established when the residual reduced below 10^{-5} for continuity and 10^{-6} for energy, velocity, and radiation. Iteration variation thresholds were set at 1° and 0.1 m/s for temperature and velocity, respectively [77]. The SIMPLE algorithm was implemented for the pressure-velocity coupling.

3.3. Validation model

The achievement of the flameless combustion regime in the simulations was verified using the temperature and oxidation factor profiles; the details are in the supplementary material. The CFD model was validated using experimental data from the SG-NG (PH) mixture combustion. Fig. 6 presents a comparison of experimental and numerical data for temperature and major species concentrations (CO, CO_2, and O_2). Temperature predictions are in good agreement with experimental data along the three lines measured, the average relative difference being less than 3.7% for all turbulence models. For CO_2 and O_2, the general trend is captured adequately, with the order of magnitude and the concentrations being consistent with the experimental data. O_2 concentrations along all lines are consistent with the flameless combustion range (2−5%) [24]. In the case of CO, only qualitative behavior is captured and all calculations overpredict the experimental results, in particular along the centerline. This stems from the EDC model's tendency to underestimate reaction rates under diluted conditions [65,81], as is the case for flameless combustion, due to the high dependence of the model constants [82,83]. Generating a higher amount of CO in the predictions, especially along the centerline

Table 3
Boundary conditions.

Boundary	Type of boundary	SG-NG (PH)	SG-NG (WPH)
Oxidizer inlet	Mass flow inlet	35.47 kg/h	
Fuel inlet		2.44 kg/h	
Inlet thermal load		136.11 kg/h	
Output thermal load	Pressure outlet	0	
Smokestack			
Ejected gases		−1120.9 Pa	0
Furnace Wall	Wall with external convection	10 W/m2-K	

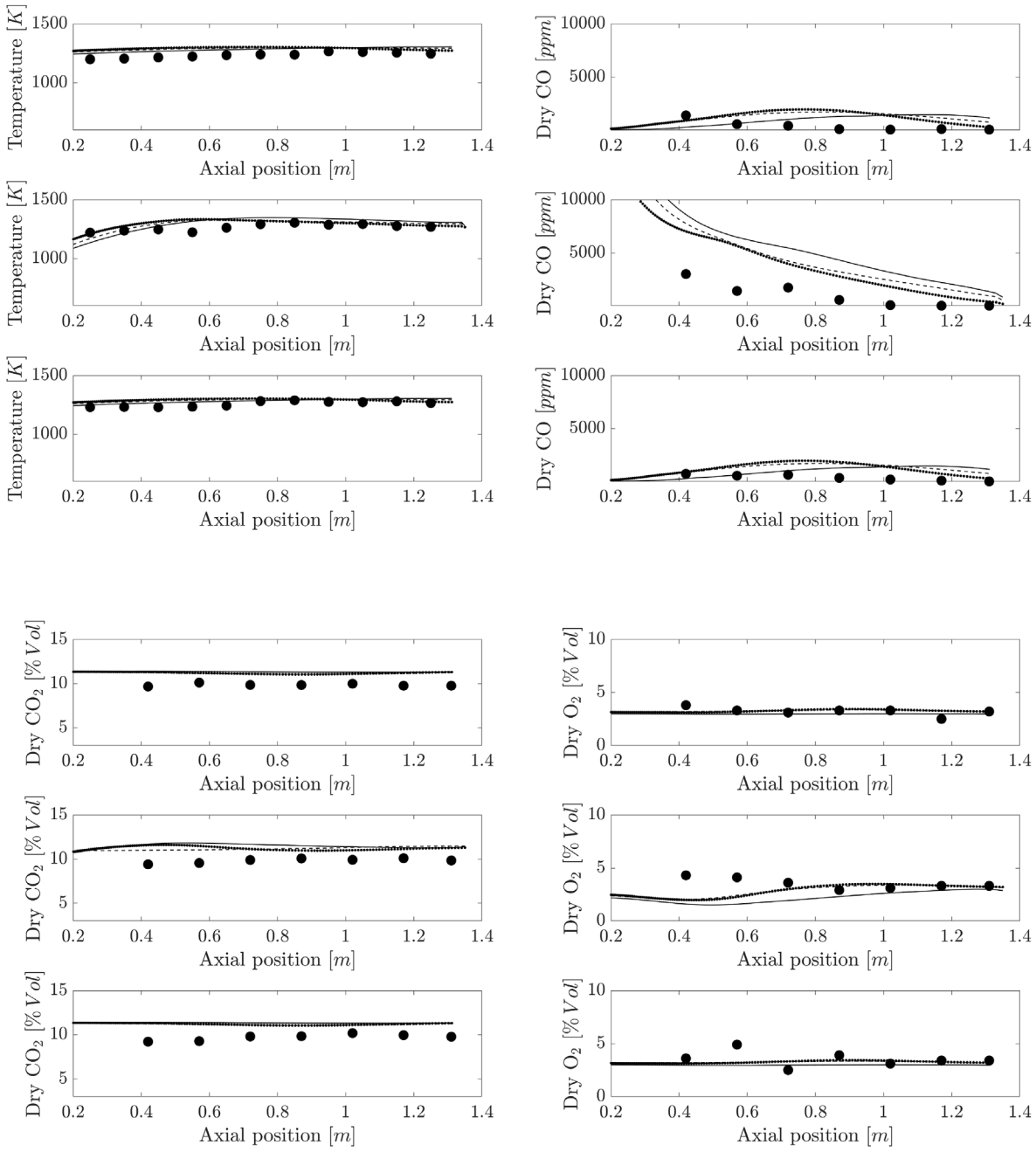

Fig. 6. Comparison of experimental (large dots) and CFD (lines) temperature and species results, using κ-ε realizable (solid line), κ-ε standard (dashed line) and κ-ε RNG (dotted line) models. Right line (upper box). Center line (central box). Left line (lower box).

where the fuel, which contains 12% CO, is discharged. Towards the end of the combustion chamber (axial distance >0.9 m), where the final reactions occur, the discrepancy decreases, indicating the limitation of the EDC model in the turbulence-chemistry interaction, producing kinetic issues in the calculated ignition and propagation reactions.

However, the agreement and uniformity in predictions for the other fields suggest that the fluid dynamics and principal aspects of flameless SG-NG mixture combustion are adequately captured by the CFD model. Moreover, as can be seen in Table 4, the simulation predicted experimental exhaust emissions adequately. The CFD model using k-ε RNG was selected for the turbulence analysis, as it produced lower deviations in species predictions.

Table 4
Exhaust emissions from the CFD Model and Experimental measures (dry basis).

Emission	CFD Model	Experimental
O2 (% by Vol.)	3.17	3.55 ± 0.24
CO2 (% by Vol.)	11.34	10.69 ± 0.68
CO (ppm)	9	18 ± 1.41

3.4. Recirculation factor (Kv)

To analyze the effect of the changes in the inlets flow when syngas is added to the fuel, the Recirculation factor (Kv) was calculated using the simulation results according to the methodology presented in Refs. [84,85] by mean of equation (4).

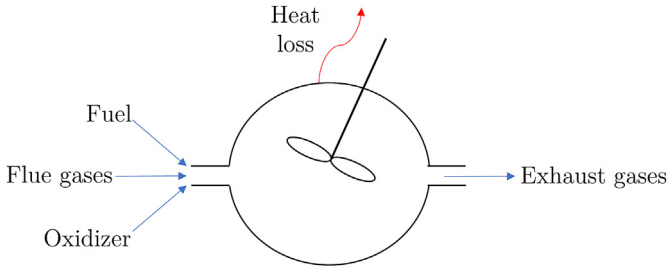

Fig. 7. Schematic diagram of a PSR.

$$K_v = \frac{\dot{m}_r - \dot{m}_{eject}}{\dot{m}_f + \dot{m}_o} \tag{4a}$$

Where $\dot{m}_r$ and are the recirculating mass flow and ejected mass flow respectively. Using the CFD simulation results, the $\dot{m}_r$ is calculated at each transverse plane as the mass flow with a negative velocity component in the x-direction.

3.5. PSR kinetic analysis

Due to high recirculation, the flameless combustion can be approximated to a Perfectly Stirred Reactor (PSR) [12,86,87]. The kinetics effects of the syngas addition at flameless combustion were analyzed using a PSR. Chemkin 2020 R2 was used for the simulation and GRI-Merch 3.0 [88] reaction mechanism was selected for the calculation. Fig. 7 schematically shows the PSR sketch, which has three mass flow inlets (fuel, oxidizer and recirculated flue gases) and one outlet. The heat losses were included taking the experimental values. The residence time was assumed to be 1 s. The rate

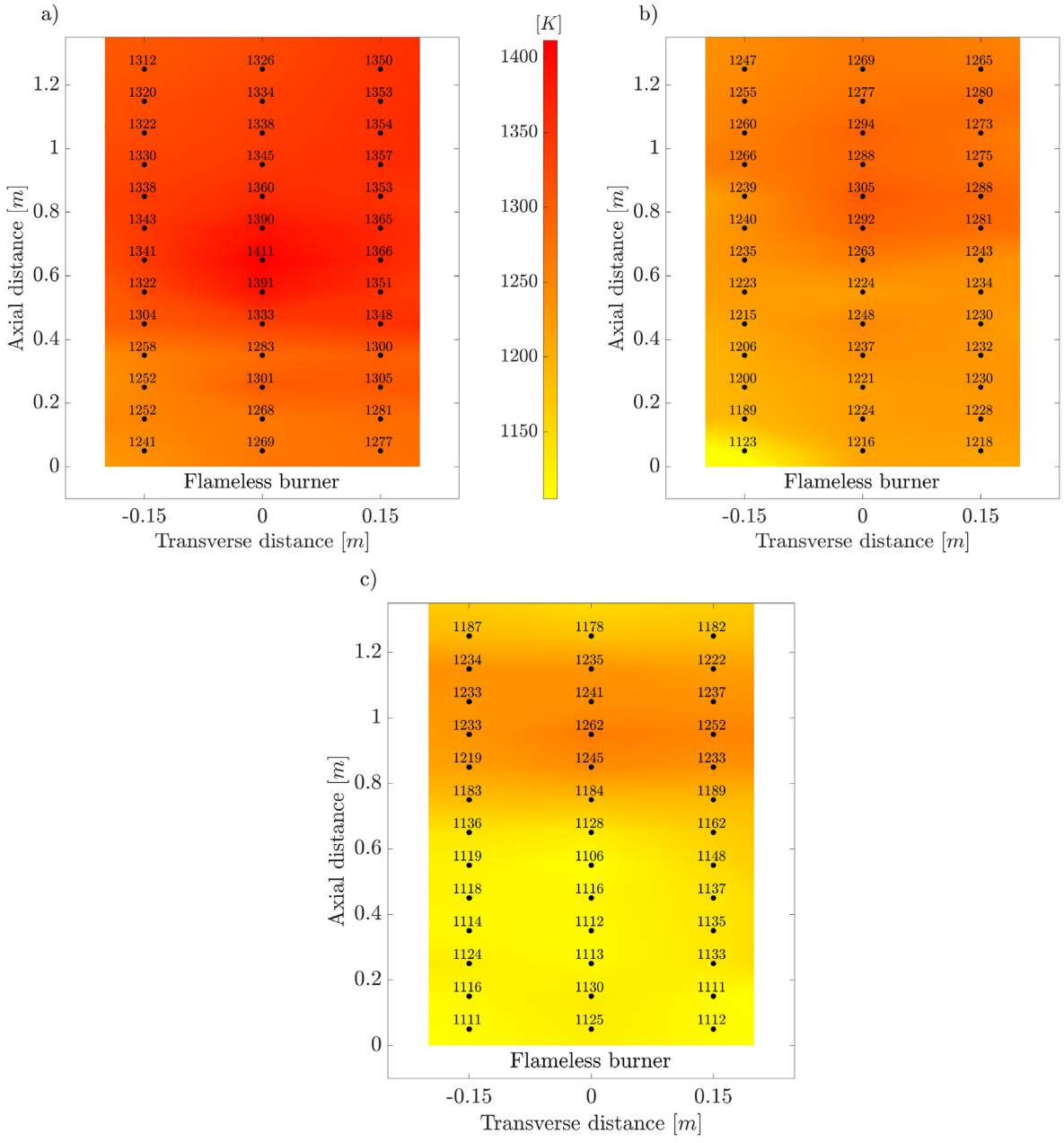

Fig. 8. Experimental temperature field in the middle plane: a) NG, b) SG-NG (PH), and c) SG-NG (WPH).

of production (ROP) obtained from PSR was used to calcuate the reaction factor ($F_{R,i}^{\pm j}$) [89].

$$F_{R,i}^{\pm j} = \frac{\mathrm{ROP}_{i,j}}{\mathrm{ROP}_{j-tot}} \times 100 \tag{4b}$$

The $\mathrm{ROP}_{i,j}$ is the rate of production of specie j from reaction i and ROP_{j-tot} is the total rate of production of specie j. The superscripts + and − represent production and consumption, respectively. The PSR approach was also used to analyze the syngas effect on NOx production at flameless combustion conditions.

4. Results and discussion

4.1. Temperature field

Fig. 8 Experimental temperature field in the middle plane: a) NG, b) SG-NG (PH), and c) SG-NG (WPH).shows the temperature contours of the middle plane according to the experimental measurements. The addition of syngas produced a general decrease in the temperatures as compared to pure NG combustion, associated with the increased recirculation due to the 37.1% higher fuel mass flow required to maintain the thermal input, which produces a momentum flux increase. Table 5 presents the maximum Kv and its axial location (x_{re}). An increase of 10.4% in Kv was found for SG-NG (PH) in comparison to pure NG. Therefore, greater dilution is expected for SG-NG (PH), leading to lower temperatures in the combustion chamber.

According to the x_{re}, the greatest recirculation occurred approximately 0.57 m from the burner for NG and SG-NG (PH). This is where the reactants converge, generating a better mix between fuel and oxidizer and therefore an increased reaction rate, producing greater heat release. The temperatures shown in Fig. 9 confirm this behavior. For SG-NG (PH), the temperature increased by 56.6 K from axial position 0.57 m to the peak at approximately 0.8 m, after which it again decreased.

For the NG case, the growth slope was greater than that of SG-NG (PH), rising almost 80 K from axial position 0.45 m to the peak at 0.65 m. That is due to the greater recirculation for SG-NG (PH), which produced an average temperature decrease of 6% in comparison to pure NG.

The upper wall temperatures of SG-NG (PH) combustion were lower than those of pure NG (see supplementary data). Additionally, due to the greater recirculation discussed previously, the CO_2 content of the flue gases also contributed to the temperature decrease when syngas was added to the fuel. According to Table 1, the SG-NG produced 12.5% more CO_2 per kW than pure NG, as confirmed by the experimental species measurements presented in Fig. 10. Considering that the specific heat of CO_2 is higher than that of N_2 (the most abundant species in flue gases), a cooling effect is produced by the increased energy storage. Furthermore, the CO_2 improves the absorptive properties, gathering more radiative energy from the reaction zone.

The RTU was calculated and compared for NG and SG-NG (PH) to determine the effect of syngas on the temperature uniformity fields (see Table 6). As can be seen, the RTU remained nearly constant. It decreased slightly in the middle plane (higher uniformity as RTU tends to zero), confirming that the addition of syngas did not alter the principal thermal characteristics of flameless combustion.

Table 5
Recirculation parameters.

Fuel	x_{re}	Kv_{max}
NG	0.5659	12.5
SG-NG (PH)	0.5730	13.8
SG-NG (WPH)	0.6067	10.6

4.2. Species profiles and exhaust emissions

CO_2 and O_2 species exhibited high uniformity for both NG and SG-NG (PH) cases. The O_2 concentrations were lower than 5%, by vol., for all cases, which is in accordance with flameless combustion. The contours are presented in the supplementary material. Fig. 10 shows the experimental CO_2 species fields. As mentioned previously, the CO_2 concentration was greater with syngas present in the fuel.

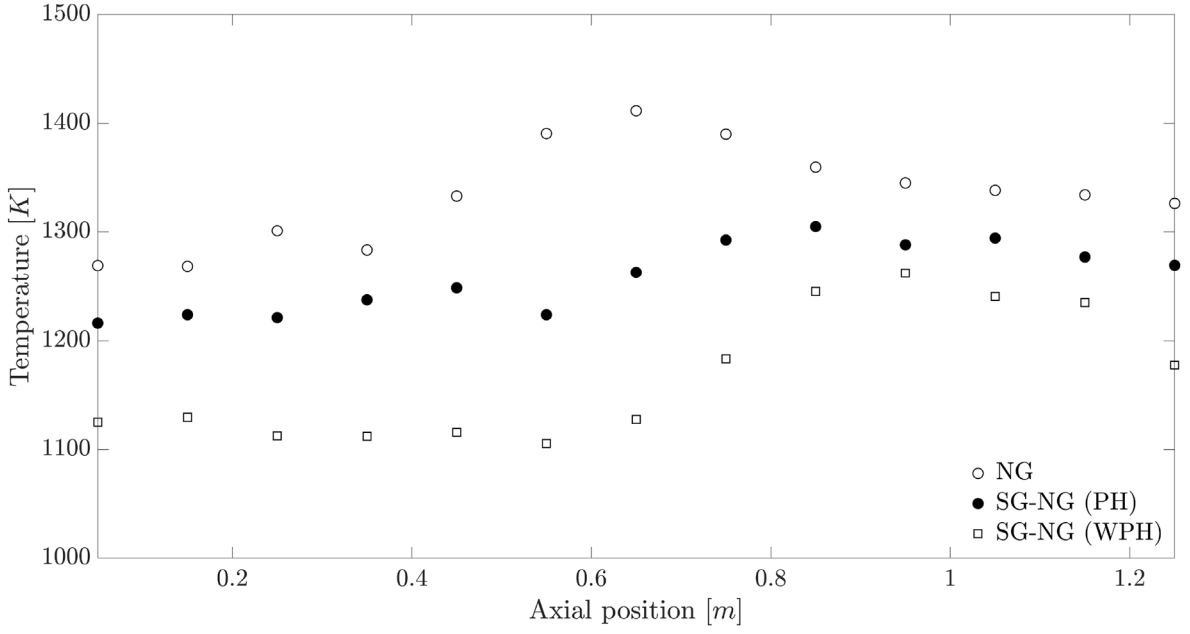

Fig. 9. Centerline temperature profiles.

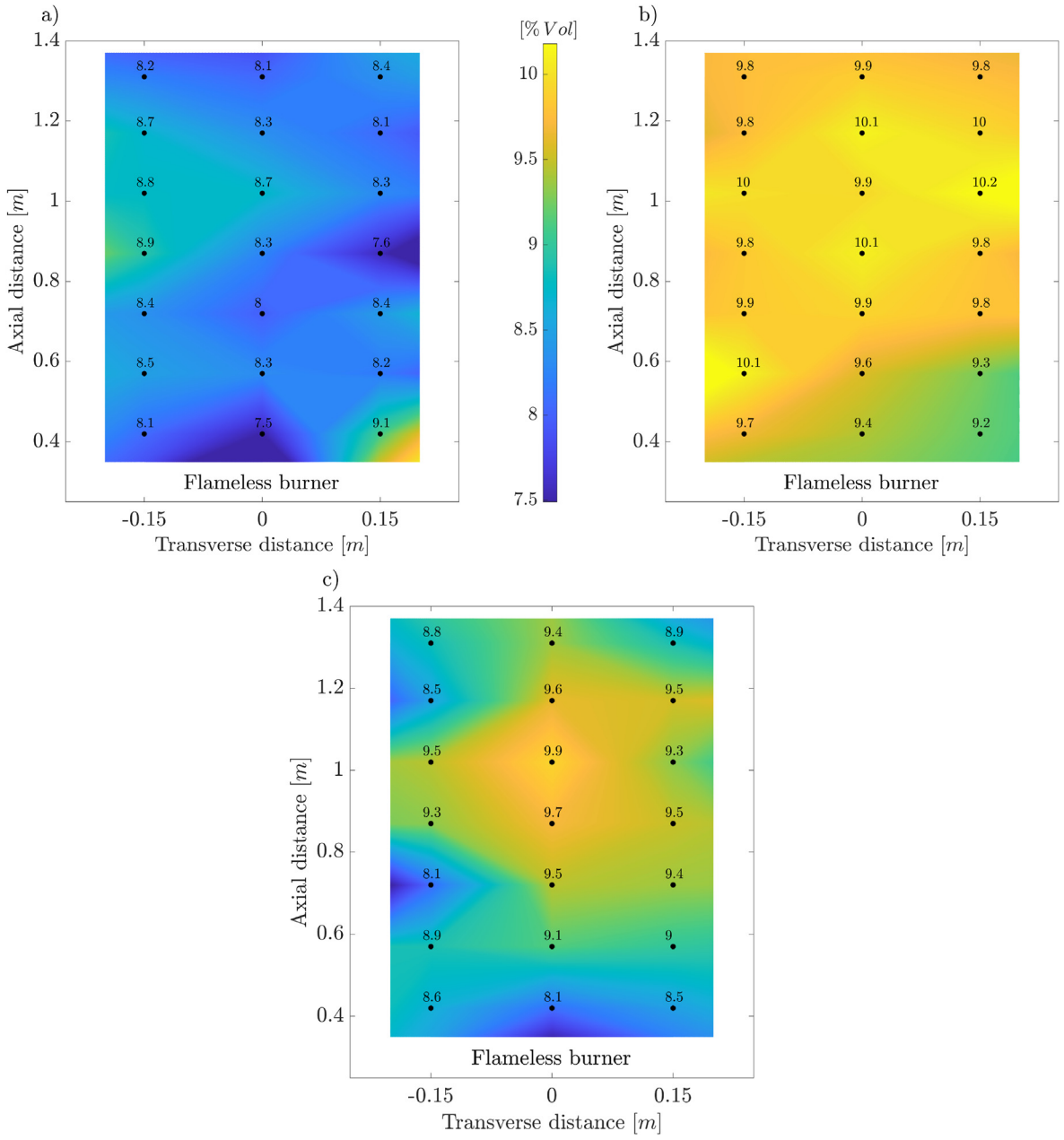

Fig. 10. Experimental CO_2 species field in the middle plane: a) NG, b) SG-NG (PH), and c) SG-NG (WPH).

Table 6
Thermal uniformity factor (RTU).

	Middle plane	Upper plane
NG	0.19	0.04
SG-NG (PH)	0.17	0.05
SG-NG (WPH)	0.28	0.04

The greater CO_2 concentration influenced the thermal fields, as mentioned in the previous section. Fig. 11 shows that along the centerline, the CO_2 concentration rose until axial position 0.8 m, decreasing thereafter for SG-NG (PH), whereas it exhibited more oscillation for pure NG. The greater recirculation and CO_2 production from fuel oxidation for SG-NG (PH) promoted homogenization in the first half of the combustion chamber. The axial positions of highest CO_2 concentrations for NG and SG-NG (PH) were 1.02 m and 0.87 m, respectively, suggesting that the reaction zone displaces towards the burner when syngas is added to the fuel. This behavior is analyzed in the next section.

As expected for O_2, the general trend along the centerline was a lower concentration for SG-NG (PH) than NG due to the lower $M_{a,stq}$ of the former. O_2 exhibits opposite behavior to CO_2 for SG-NG (PH), decreasing until axial position 0.82 m due to its consumption by fuel oxidation, after which it increased until the chamber's end due to the recirculation.

Conversely to CO_2 and O_2 species fields, CO does not exhibit uniform behavior, and furthermore shows greater concentrations

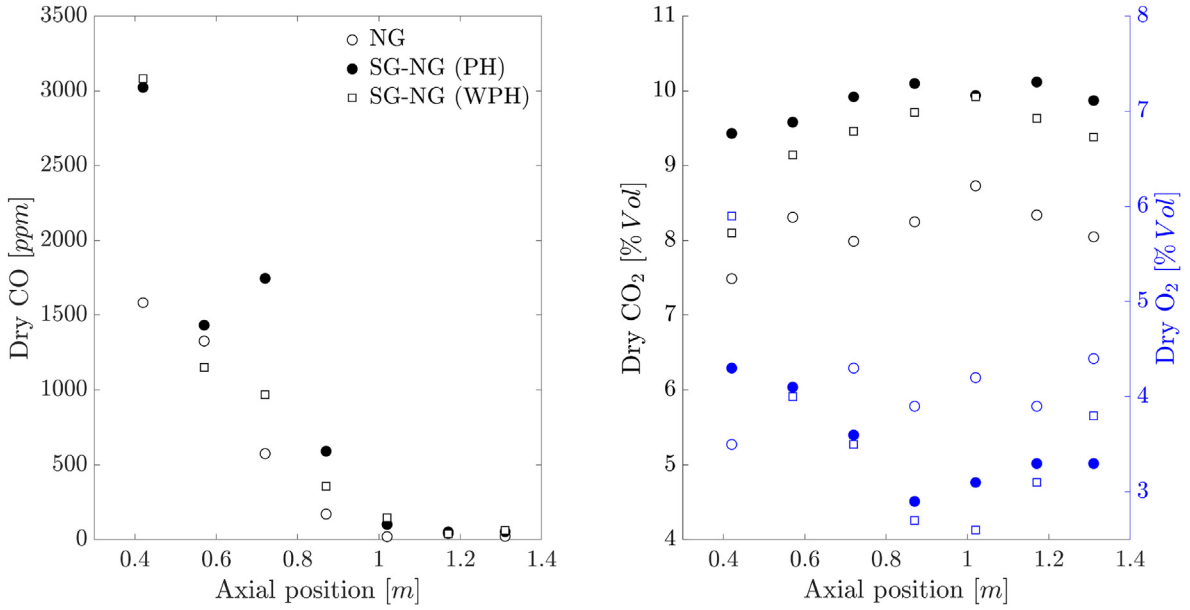

Fig. 11. Species concentration along the centerline.

prior to axial position 0.6 m along the centerline. However, this is expected due to CH_4 oxidation for both NG and SG-NG, as well as syngas' CO content in the latter. In general, the CO concentration is always higher for SG-NG than for NG, as presented in Fig. 12. While an obvious explanation is the initial CO content of the SG-NG mixture, this is not the only factor. The H_2 content accelerates the reaction, increasing production of OH and H radicals; consequently, more CH_4 is oxidized to CO for SG-NG (PH) as compared to NG.

The higher concentrations over nearly half of the middle plane are associated with the distributed reaction zone of flameless combustion. Nevertheless, the CO concentration decreases towards the combustion chamber's end, with the experimental smokestack emissions (<10 ppm, see Fig. 14) confirming complete combustion.

Measured NOx concentrations were below 10 ppm for all cases (see supplementary material). Fig. 13 shows the NOx concentration along the centerline, indicating a lower concentration for SG-NG (PH) than NG. This behavior suggests a change in the reaction pathways of NOx production. According to the PSR results, the thermal route contribution decreased from 8.85% to 7.16% for SN-NG compared to NG. This reduction is evidently due to the temperature decrease when syngas is added. Indeed, NOx was near zero (<2 ppm) throughout the middle plane for SG-NG (WPH), where the lowest temperatures were obtained.

However, an average decrease of around 50% was observed for SG-NG as compared to NG; therefore, not only the thermal route is affected when syngas is present in the fuel. The NOx formation pathway routes were analyzed using the reaction factors $F_{R,i}^{\pm NO}$, $F_{R,i}^{\pm NO_2}$ and $F_{R,i}^{\pm N_2}$. According to $F_{R,i}^{-N_2}$ the three principal reactions are $N_2 + O + M \rightarrow N_2O + M$ (R185), $N_2 + H \rightarrow NNH$ (R204) and $N_2 + H + M \rightarrow NNH + M$ (R205), suggesting that the principal routes are the N2O and NNH routes. Excluding the recombinations reactions among NO and NO_2, the higher reaction factor is the $F_{R,182}^{+NO}$ corresponding to the reaction $N_2O + O \rightarrow NO + NO$, confirming that the principal is the N_2O route. This behavior is the same for SG-NG and NG. However, the magnitude of the ROP for R185, R204 and R205 decrease by 10.52%, 10.71% and 6.62% when syngas is added to the fuel. According to sensibility analysis, the principal reaction that influences the H consumption is the $H + O_2 + H_2O \rightarrow HO_2 + H_2O$ (R35) for both SG-NG and NG, but the $F_{R,35}^{-H}$ is higher, around 2% for SN-NG respect to NG. The higher amount of H2 in the SG-NG promotes the reaction rate of R35 and therefore the consumption of H, leaving fewer H radicals available to the reactions R185, R204 and R205 to produce NO although N_2O and NNH routes. According to these results, the addition of 30% syngas did not promote other NOx formations pathways (NNH, prompt, and N_2O intermediate routes).

Finally, the smokestack emissions are presented in Fig. 14 Measured exhaust gases at smokestack. As expected, CO_2 emissions were higher, while CO emissions were 24% lower, for SG-NG (PH), as compared to pure NG. In both cases, NOx emissions were below 3.9 ppm, indicating that the addition of syngas did not have a considerable effect on this contaminant. The same emissions values were registered in the flue gases evacuated through the regeneration system. The percent of ejected gases by the regenerator remains almost constant among NG and SG-NG(PH), with values of 54% and 55%, respectively.

4.3. Reaction zone

Spontaneous chemiluminescence was used to image the reaction zone inside the furnace. The images captured by the ICCD camera through Windows 1 (nearest burner) and 2 (downstream), for NG and SG-NG (PH), are presented in Fig. 15. According to the wavelengths transmitted by the filter, the emissions captured may correspond to CH, CH_2O, and HCO radicals [61–64]. The radical emissions intensity appeared higher for SG-NG than for NG when viewed through window 1, whereas the opposite occurred through window 2, which is nearer the chamber's end, suggesting a lower presence of radicals further downstream for SG-NG combustion. On the other hand, the intensity at window 2 is comparable with

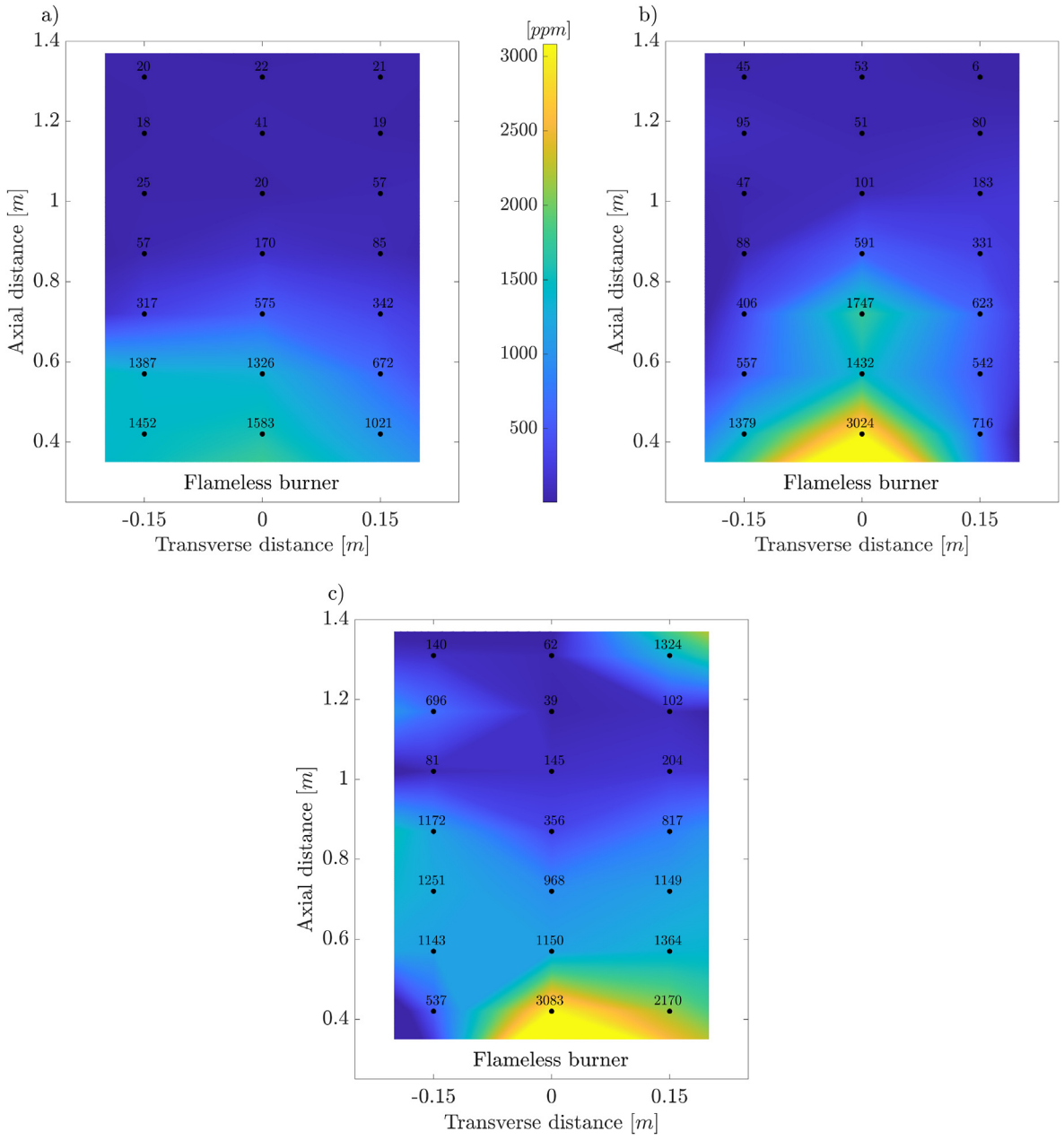

Fig. 12. Experimental CO species field in the middle plane: a) NG, b) SG-NG (PH), and c) SG-NG (WPH).

window 1 in the NG case. This behavior indicates the translation of the reaction zone towards the burner when syngas is added to the fuel.

The H_2 content of the SG-NG mixture increases OH and H radical concentrations, promoting the branching reactions and increasing the reaction rates. The subtraction of hydrogen from CH4 to produce CH3 is principally by $OH + CH_4 \rightarrow CH_3 + H_2O$ (R98) according to the $F_{R,i}^{-CH_4}$ and $F_{R,i}^{+CH_3}$. The sensibility analysis reveals that the R35 is the reaction that most favors the CH3 for both SG-NG and NG. However, the sensibility factor increases around 13.4% when syngas is added to the fuel due to the higher production of H radicals and, therefore, promotes the hydrogen subtraction from CH_4. The CH2O is relevant as a tracer from the reaction zone at lower and intermediate temperatures. For NG, the most important reaction in the CH_2O production according to $F_{R,i}^{+CH_2O}$ is $CH_2 + O_2 \rightarrow O + CH_2O$ (R291) whereas, for the SG-NG changes to $CH_3O + M \rightarrow H + CH_2O$ (R57). This change is produced by $F_{R,105}^{+CH_3O}$ increase of the $OH + CH_3OH \rightarrow CH_3O + H_2O$ (R105) from 79.7% to 82.4%, due to high OH available for SG-NG. Consequently, the oxidation process continues by the route HCO- > CO- > CO_2, by mean of the reactions $OH + CH_2O \rightarrow HCO + H_2O$ (R101), $HCO + O_2 \rightarrow HO_2 + CO$ (R168), $HCO + H_2O \rightarrow H + CO + H_2O$ (R166) and $HCO + M \rightarrow H + CO + M$ (R167) according to the $F_{R,i}^{\pm HCO}$.

On the other hand, the greater OH and CO_2 concentrations for SG-NG increase the reaction rates of the other pathways producing

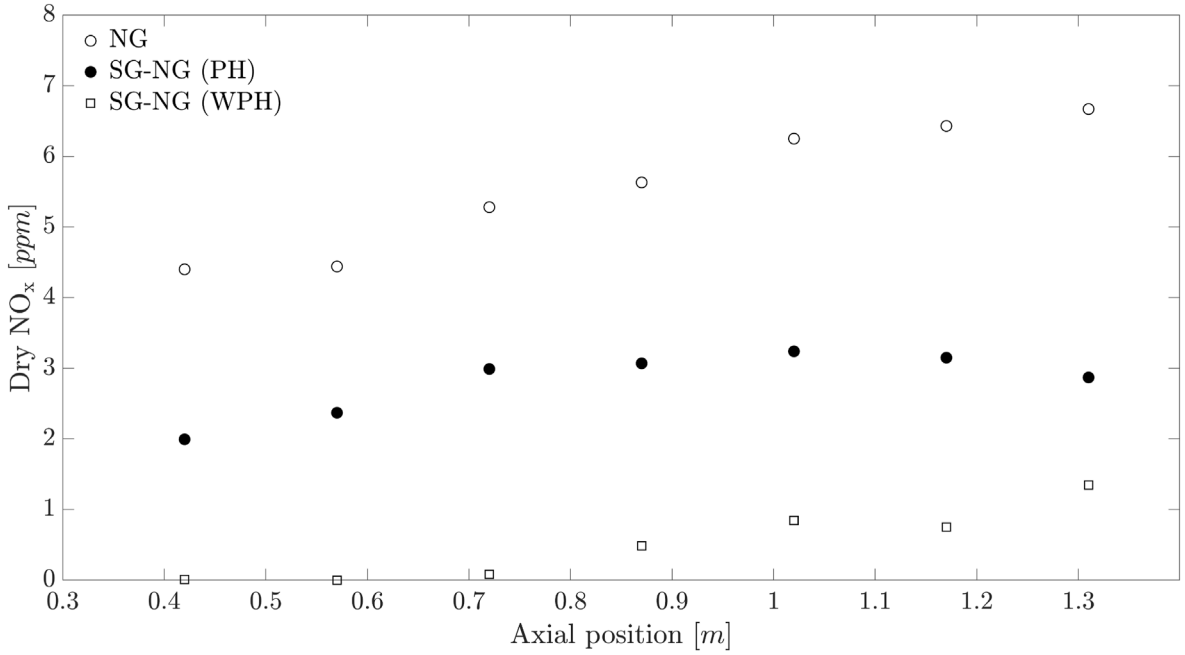

Fig. 13. NOx concentration along the centerline.

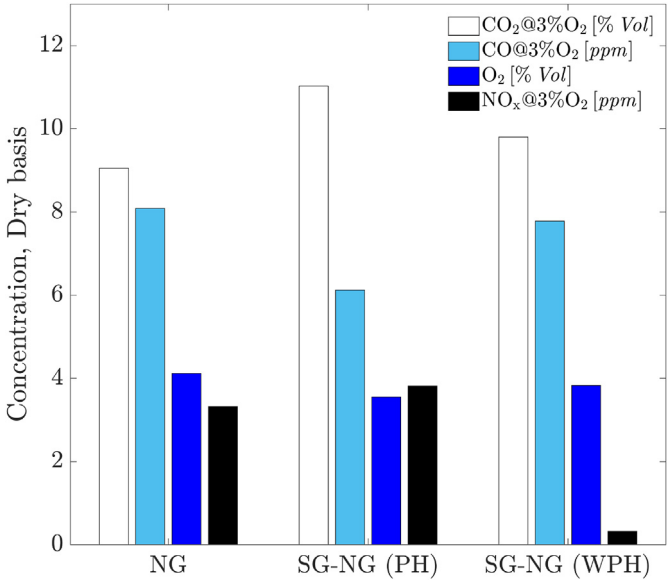

Fig. 14. Measured exhaust gases at smokestack.

CH_2O through reactions $CH_2(S) + CO_2 \rightarrow CH_2O + CO$ (R153) [90,91], increasing the $F_{R,153}^{\pm CH_2}$ from 16% to 18% when syngas is added to the fuel. Globally, these effects move the reaction zone towards the burner for SG-NG.

According to previous reaction pathways, higher CH_2O concentrations are expected nearer the burner for SG-NG. Considering that this species is a good indicator of the reaction zone for flameless combustion [59,60], it is likely that most captured light by the ICCD camera corresponds to CH_2O emissions, even though the filter used is not precisely calibrated for this species. However, this possibility requires further rigorous study, which is beyond the scope of this paper.

4.4. Effect of oxidizer preheating

An additional test was carried out using the SG-NG mixture without oxidizer preheating (WPH), with the regenerative system disabled. All flue gases were consequently evacuated through the smokestack as the outflow of flue gas through the regenerators system was disengaged. All operating parameters were the same as for SG-NG (PH). According to the thermal and species fields, along with visual observations inside the combustion chamber, flameless SG-NG combustion was achieved without oxidizer preheating and no further geometrical or operative changes. However, changes in the thermal field and fluid dynamics were observed in comparison to SG-NG (PH).

As shown in Fig. 8, the SG-NG (WPH) temperatures were the lowest of the three cases studied, on average being 6% below those of SG-NG (PH). Contrary to the other tests, for SG-NG (WPH) the temperature increased more than 100 K along the centerline from the first to the second half of the combustion chamber. This temperature increase diverges from the thermal uniformity of flameless combustion, as indicated by the RTU increasing by about 65% as compared to SG-NG (PH). This suggests the possibility of small conventional flames, although they were not visually observed. Moreover, the greatest temperature along the centerline for SG-NG (WPH) was around axial position 0.95 m, almost 40 cm and 10 cm further downstream than for NG and SG-NG (PH), respectively, indicating that the reaction zone had translated towards the combustion end wall.

Fig. 16 compares the chemiluminescence of PH and WPH conditions. The intensity was graduated distinctly for each window to improve the visualization. The emission intensity decreased at window 1 for the WHP case, indicating that radicals production

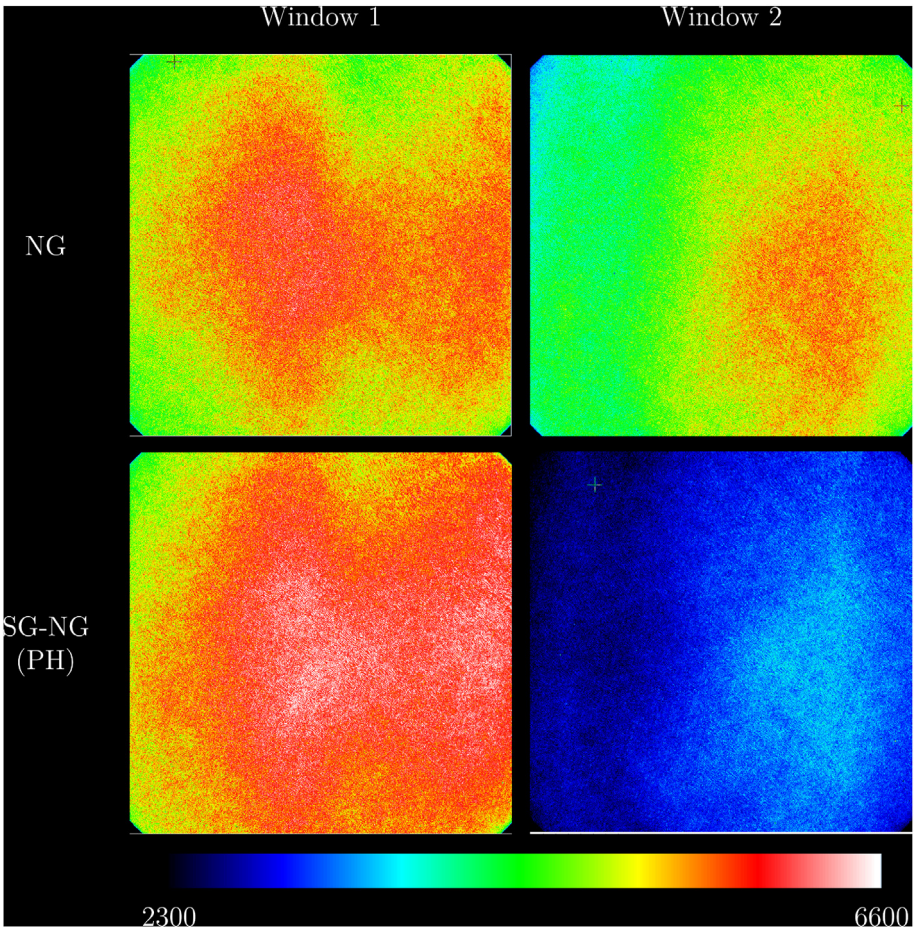

Fig. 15. CH* chemiluminescence inside the combustion chamber for NG and SG-NG (PH).

(CH_2O, HCO, and CH) was reduced compared to the PH case. The trend was the same for window 2, although the decrease was smaller, suggesting relatively higher radical production in this zone.

The disengaged regeneration was the primary cause for the described changes. The energy previously recovered to preheat the oxidizer was instead lost with the exhaust gases, resulting in lower temperatures and consequently decreased reaction rates. However, this does not directly explain the translation of the reaction rate zone and the greater temperature delta between the first and second halves of the combustion chamber. Rather, these effects stem from changes in the fluid dynamics due to the absence of the outflow of flue gas through the regenerators. Without ejection, the recirculation and the mixing of the oxidizer-fuel with the flue gases are entirely driven by the jet discharges. Furthermore, with the lower temperature, the inlet air velocity is reduced as compared to the PH case, and the drag effect is weakened, decreasing the amount of recirculating gases. According to the K_{vmax} values presented in Table 5 for PH and WPH, around a 23% decrease occurs with the outflow of flue gas through the regenerators is disabled. Using the CFD model, the $\dot{m}_r$ flow was calculated, presented in Fig. 17, finding $\dot{m}_r$ to be higher with PH across all combustion chamber positions. The recirculation zones are similar in both cases (see supplementary material), although the velocity along the axial direction decreased for the WPH case, as shown in Fig. 18, resulting in a reduction of recirculating gases.

Due to the lower recirculation, the confluence reactants point moves towards the end wall. Furthermore, the lower temperature of the tripartite mix (fuel-oxidizer-flue gases) increases the ignition delay time and translates the reaction zone downstream. Finally, when the principal heat release occurs, the lower dilution of the reactants, due to decreased recirculation, results in greater temperature increase in the last quarter of the combustion chamber.

5. Conclusions

The effect of the addition of syngas to natural gas in a regenerative furnace under flameless combustion conditions was studied numerically and experimentally. The semi-industrial furnace was originally designed to operate with natural gas and no geometrical modifications were made. Temperature and species inside the combustion chamber were measured using specific sample probes. Spontaneous chemiluminescence was imaged as an indicator of reaction zone location. The effect of oxidizer preheating was also analyzed with syngas added to the fuel. The results lead to the following conclusions:

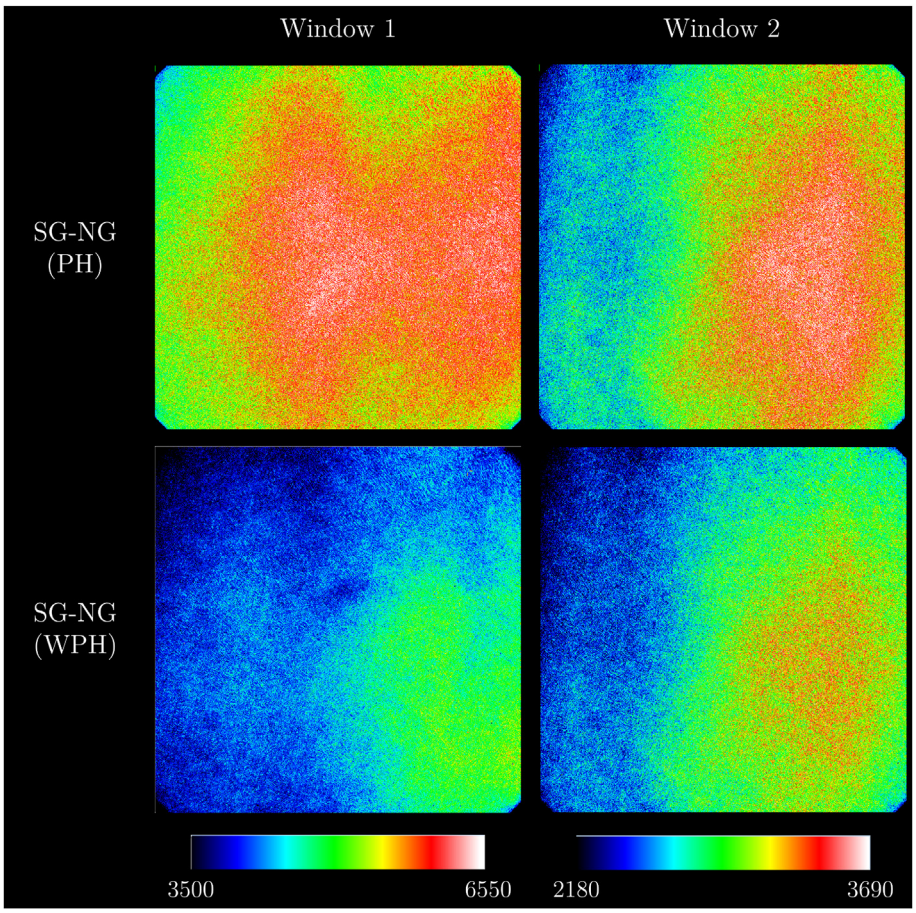

Fig. 16. CH* chemiluminescence inside the combustion chamber for SG-NG (PH) and (WPH).

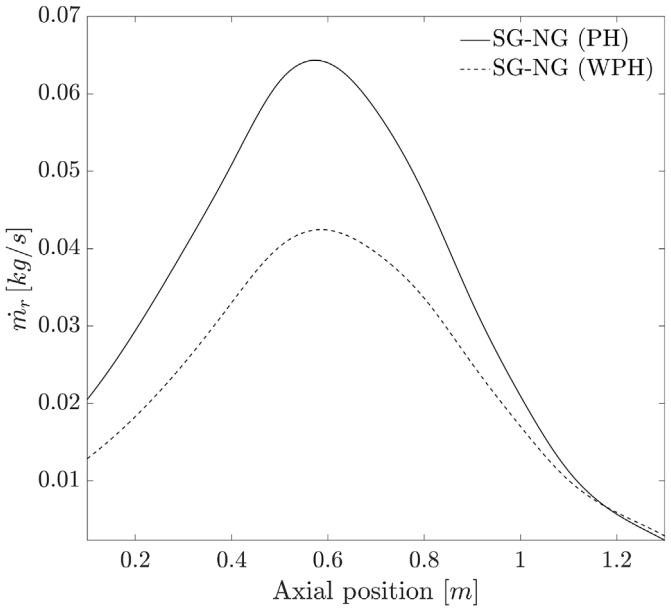

Fig. 17. Recirculating mass flow.

- Stable flameless combustion conditions can be achieved using 30% (by vol.) of syngas mixture without any geometrical or operational modification in a semi-industrial regenerative furnace.
- The furnace temperature decreases when syngas is added to the fuel due to higher recirculation and increased CO_2 in the flue gases. However, the thermal uniformity of flameless combustion remains and tends to be highest in the middle plane (RTU decreases by 10.5%).
- The high uniformity of temperature and species profiles, along with the low pollution (CO and NOx) emissions characteristic of flameless combustion, are conserved with a 30% syngas 70% natural gas fuel mixture.
- NOx production decreases when syngas is added to the natural gas due to a combined effect on the thermal, N2O, and NNH formation routes. The lower temperature reduces the thermal contribution by about 1.7% and the higher consumption of H radical by R35 when syngas is added, produces a lower availability of this element to the reactions R185, R204 and R205 associated with the N_2O and NNH reaction pathways.
- The addition of syngas moves the reaction zone upstream due to the increased production of OH and H radicals, which subsequently accelerate the CH_2O production routes.
- Flameless combustion conditions can be achieved without oxidizer preheating using a 30% syngas and 70% natural gas fuel mixture. However, the thermal uniformity decreases, as indicated by the RTU increasing approximately 65% as compared to SG-NG (PH) and the temperature rise of more than 100 K from the first to the second half of the combustion chamber, due to the lower reactant dilution.

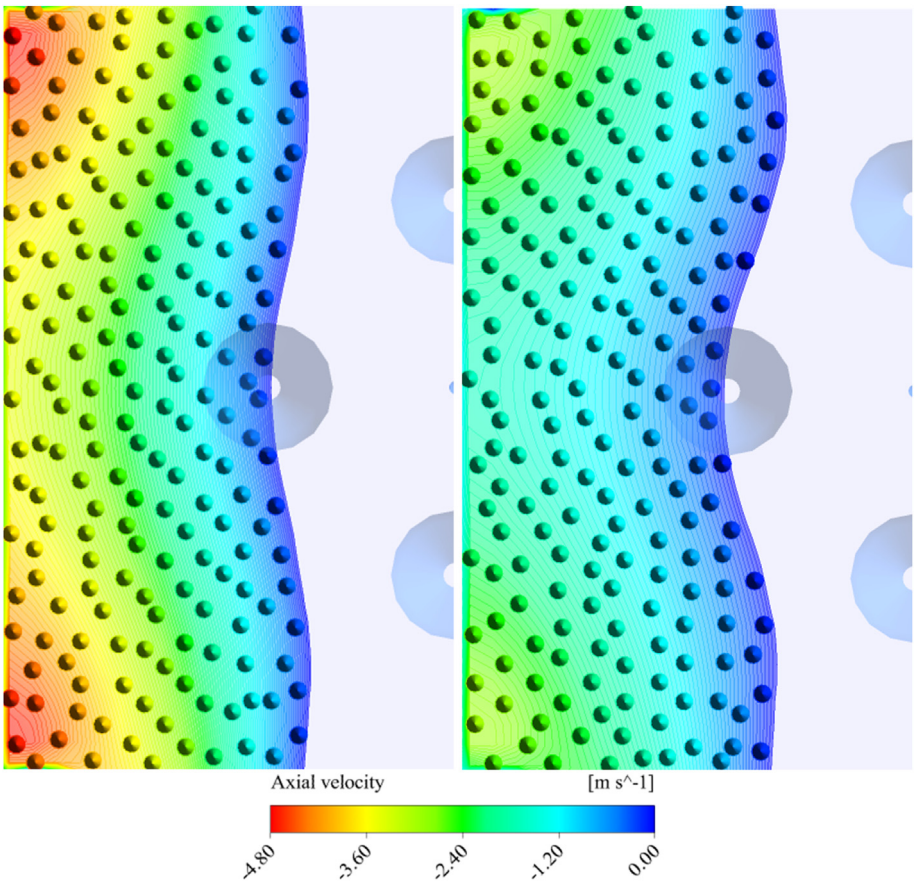

Fig. 18. Axial velocity of recirculating gases (from burner point of view). PH (left). WPH (right).

- The absence of outflow of flue gas through the regenerators and the lower velocities when operating without preheating decrease the recirculation flow by approximately 23%. However, the locations of recirculation zones do not change between (PH) and (WPH).
- The reduced recirculation delays reactant mixing and ignition, resulting in the reaction zone translating downstream inside the combustion chamber.

Credit author statement

Hernando A. Yepes: Conceptualization, Methodology, Software, Validation, Formal analysis, Investigation, Writing – original draft, Visualization Julian E. Obando: Investigation Andres A. Amell: Conceptualization, Methodology, Resources, Formal analysis, Writing – review & editing, Supervision, Funding acquisition,

Declaration of competing interest

The authors declare that they have no known competing financial interests or personal relationships that could have appeared to influence the work reported in this paper.

Acknowledgements

The authors gratefully acknowledge the financial support provided by the Colombia Scientific Program within the framework of the call Ecosistema Científico (Contract No. FP44842-218-2018).

Appendix A. Supplementary data

Supplementary data to this article can be found online at https://doi.org/10.1016/j.energy.2022.124008.

References

[1] Chiari L, Zecca A. Constraints of fossil fuels depletion on global warming projections. Energy Pol 2011;39:5026–34. https://doi.org/10.1016/j.enpol.2011.06.011.
[2] Sabia P, de Joannon M, Fierro S, Tregrossi A, Cavaliere A. Hydrogen-enriched methane Mild Combustion in a well stirred reactor. Exp Therm Fluid Sci 2007;31:469–75. https://doi.org/10.1016/j.expthermflusci.2006.04.016.
[3] García-Armingol T, Ballester J. Operational issues in premixed combustion of hydrogen-enriched and syngas fuels. Int J Hydrogen Energy 2015;40:1229–43. https://doi.org/10.1016/j.ijhydene.2014.11.042.
[4] Ranjan R, Clemens NT. Insights into flashback-to-flameholding transition of hydrogen-rich stratified swirl flames. Proc Combust Inst 2020. https://doi.org/10.1016/j.proci.2020.06.017.
[5] Weber R, Smart JP, Kamp W Vd. 2ee on the (MILD) combustion of gaseous, liquid, and solid fuels in high temperature preheated air. Proc Combust Inst 2005;30 II:2623–9. https://doi.org/10.1016/j.proci.2004.08.101.
[6] Cavaliere A, de Joannon M. Mild combustion. Prog Energy Combust Sci 2004;30:329–66. https://doi.org/10.1016/j.pecs.2004.02.003.
[7] Wünning J. Flameless oxidation to reduce thermal no-formation. Prog Energy Combust Sci 1997;23:81–94. https://doi.org/10.1016/S0360-1285(97)00006-3.
[8] Effuggi A, Gelosa D, Derudi M, Rota R. Mild combustion of methane-derived fuel mixtures: natural gas and biogas. Combust Sci Technol 2008;180:481–93. https://doi.org/10.1080/00102200701741368.
[9] Huang M, Li R, Xu J, Cheng S, Deng H, Zhang B, et al. Effect of thermal input, excess air coefficient and combustion mode on natural gas MILD combustion in industrial-scale furnace. Fuel 2021;302:121179. https://doi.org/10.1016/J.FUEL.2021.121179.
[10] Perrone D, Castiglione T, Klimanek A, Morrone P, Amelio M. Numerical simulations on Oxy-MILD combustion of pulverized coal in an industrial boiler. Fuel Process Technol 2018;181:361–74. https://doi.org/10.1016/

J.FUPROC.2018.09.001.
[11] Cho ES, Shin D, Lu J, de Jong W, Roekaerts DJEM. Configuration effects of natural gas fired multi-pair regenerative burners in a flameless oxidation furnace on efficiency and emissions. Appl Energy 2013;107:25–32. https://doi.org/10.1016/J.APENERGY.2013.01.035.
[12] Yu Y, Gaofeng W, Qizhao L, Chengbiao M, Xianjun X. Flameless combustion for hydrogen containing fuels. Int J Hydrogen Energy 2010;35:2694–7. https://doi.org/10.1016/j.ijhydene.2009.04.036.
[13] Mardani A, Tabejamaat S. Effect of hydrogen on hydrogen-methane turbulent non-premixed flame under MILD condition. Hyceltec 2009 Conf 2010;35:11324–31. https://doi.org/10.1016/j.ijhydene.2010.06.064.
[14] Wang F, Mi J, Li P, Zheng C. Diffusion flame of a CH 4/H 2 jet in hot low-oxygen coflow. Int J Hydrogen Energy 2011;6:9267–77. https://doi.org/10.1016/j.ijhydene.2011.04.180.
[15] Mardani A, Tabejamaat S, Hassanpour S. Numerical study of CO and CO2 formation in CH4/H2 blended flame under MILD condition. Combust Flame 2013;160:1636–49. https://doi.org/10.1016/j.combustflame.2013.04.003.
[16] Sepman A, Abtahizadeh E, Mokhov A, Van Oijen J, Levinsky H, De Goey P. Experimental and numerical studies of the effects of hydrogen addition on the structure of a laminar methane-nitrogen jet in hot coflow under MILD conditions. Int J Hydrogen Energy 2013;38:13802–11. https://doi.org/10.1016/j.ijhydene.2013.08.015.
[17] Mardani A, Karimi Motaalegh Mahalegi H. Hydrogen enrichment of methane and syngas for MILD combustion. Int J Hydrogen Energy 2019;44:9423–37. https://doi.org/10.1016/J.IJHYDENE.2019.02.072.
[18] Ebrahimi Fordoei E, Mazaheri K. Effects of preheating temperature and dilution level of oxidizer, fuel composition and strain rate on NO emission characteristics in the syngas moderate or intense low oxygen dilution (MILD) combustion. Fuel 2021;285:119118. https://doi.org/10.1016/j.fuel.2020.119118.
[19] Boussetla S, Mameri A, Hadef A. NO emission from non-premixed MILD combustion of biogas-syngas mixtures in opposed jet configuration. Int J Hydrogen Energy 2021. https://doi.org/10.1016/j.ijhydene.2021.01.074.
[20] Ali G, Zhang T, Wu W, Zhou Y. Effect of hydrogen addition on NOx formation mechanism and pathways in MILD combustion of H2-rich low calorific value fuels. Int J Hydrogen Energy 2020;45:9200–10. https://doi.org/10.1016/j.ijhydene.2020.01.027.
[21] Salavati-Zadeh A, Esfahanian V, Nourani Najafi SB, Saeed H, Mohammadi M. Kinetic simulation of flameless burners with methane/hydrogen blended fuel: effects of molecular diffusion and Schmidt number. Int J Hydrogen Energy 2018;43:5972–83. https://doi.org/10.1016/J.IJHYDENE.2017.11.149.
[22] Cheong KP, Wang G, Wang B, Zhu R, Ren W, Mi J. Stability and emission characteristics of nonpremixed MILD combustion from a parallel-jet burner in a cylindrical furnace. Energy 2019;170:1181–90. https://doi.org/10.1016/j.energy.2018.12.146.
[23] Mao Z, Zhang L, Zhu X, Zheng C. Experiment investigation of coal MILD-Oxy combustion integrated with flue gas recirculation at a 0.3 MWth furnace. Fuel Process Technol 2017;162:126–34. https://doi.org/10.1016/j.fuproc.2017.04.002.
[24] Hu F, Li P, Guo J, Wang F, Wang K, Jiang X, et al. Optimal equivalence ratio to minimize NO emission during moderate or intense low-oxygen dilution combustion. Energy Fuel 2018;32:4478–92. https://doi.org/10.1021/acs.energyfuels.7b03162.
[25] Xie M, Dai F, Tu Y. A numerical study of accelerated moderate or intense low-oxygen dilution (MILD) combustion stability for methane in a lab-scale furnace by off-stoichiometric combustion technology. Chin J Chem Eng 2021;32:108–18. https://doi.org/10.1016/j.cjche.2020.09.053.
[26] Khalil AEE, Gupta AK. The role of CO2on oxy-colorless distributed combustion. Appl Energy 2017;188:466–74. https://doi.org/10.1016/j.apenergy.2016.12.048.
[27] Veríssimo AS, Rocha AMA, Costa M. Importance of the inlet air velocity on the establishment of flameless combustion in a laboratory combustor. Exp Therm Fluid Sci 2013;44:75–81. https://doi.org/10.1016/j.expthermflusci.2012.05.015.
[28] Xie Y, Tu Y, Jin H, Luan C, Wang Z, Liu H. Numerical study on a novel burner designed to improve MILD combustion behaviors at the oxygen enriched condition. Appl Therm Eng 2019;152:686–96. https://doi.org/10.1016/J.APPLTHERMALENG.2019.02.023.
[29] Xu S, Tu Y, Huang P, Luan C, Wang Z, Shi B, et al. Effects of wall temperature on methane MILD combustion and heat transfer behaviors with non-preheated air. Appl Therm Eng 2020;174:115282. https://doi.org/10.1016/j.applthermaleng.2020.115282.
[30] Li Z, Tomasch S, Chen ZX, Parente A, Ertesvåg IS, Swaminathan N. Study of MILD combustion using LES and advanced analysis tools. In: Proc. Combust. Inst., vol. 38. Elsevier Ltd; 2021. p. 5423–32. https://doi.org/10.1016/j.proci.2020.06.298.
[31] Jigjid K, Tamaoki C, Minamoto Y, Nakazawa R, Inoue N, Tanahashi M. Data driven analysis and prediction of MILD combustion mode. Combust Flame 2021;223:474–85. https://doi.org/10.1016/j.combustflame.2020.10.025.
[32] Aanjaneya K, Chen Y, Cao W, Borgnakke C, Atreya A. A numerical study of localized swirling injection of oxidizer for homogeneous combustion with oxygen enrichment. Fuel 2021;283:118773. https://doi.org/10.1016/j.fuel.2020.118773.
[33] Khalil HM, Eldrainy YA, Abdelghaffar WA, Abdel-Rahman AA. Increased heat transfer to sustain flameless combustion under elevated pressure conditions – a numerical study. Eng Appl Comput Fluid Mech 2019;13:782–803. https://doi.org/10.1080/19942060.2019.1645737.
[34] Zhu Z, Xiong Y, Zheng X, Chen W, Ren B, Xiao Y. Experimental and numerical study of the effect of fuel/air mixing modes on NOx and CO emissions of MILD combustion in a boiler burner. J Therm Sci 2021;30:656–67. https://doi.org/10.1007/s11630-020-1323-1.
[35] Derudi M, Villani A, Rota R. Sustainability of mild combustion of hydrogen-containing hybrid fuels. Proc Combust Inst 2007;31 II:3393–400. https://doi.org/10.1016/j.proci.2006.08.107.
[36] Parente A, Galletti C, Tognotti L. Effect of the combustion model and kinetic mechanism on the MILD combustion in an industrial burner fed with hydrogen enriched fuels. Int J Hydrogen Energy 2008;33:7553–64. https://doi.org/10.1016/j.ijhydene.2008.09.058.
[37] Galletti C, Parente A, Derudi M, Rota R, Tognotti L. Numerical and experimental analysis of NO emissions from a lab-scale burner fed with hydrogen-enriched fuels and operating in MILD combustion. Int J Hydrogen Energy 2009;34:8339–51. https://doi.org/10.1016/j.ijhydene.2009.07.095.
[38] Arghode VK, Gupta AK. Hydrogen addition effects on methane-air colorless distributed combustion flames. Int J Hydrogen Energy 2011;36:6292–302. https://doi.org/10.1016/j.ijhydene.2011.02.028.
[39] Ayoub M, Rottier C, Carpentier S, Villermaux C, Boukhalfa AM, Honoré D. An experimental study of mild flameless combustion of methane/hydrogen mixtures. Int J Hydrogen Energy 2012;37:6912–21. https://doi.org/10.1016/j.ijhydene.2012.01.018.
[40] Li P, Wang F, Mi J, Dally BB, Mei Z, Zhang J, et al. Mechanisms of NO formation in MILD combustion of CH4/H2 fuel blends. Int J Hydrogen Energy 2014;39:19187–203. https://doi.org/10.1016/j.ijhydene.2014.09.050.
[41] Chinnici A, Nathan GJ, Dally BB. Combined solar energy and combustion of hydrogen-based fuels under MILD conditions. Int J Hydrogen Energy 2018;43:20086. https://doi.org/10.1016/j.ijhydene.2018.09.027. –100.
[42] Cellek MS. Flameless combustion investigation of CH4/H2 in the laboratory-scaled furnace. Int J Hydrogen Energy 2020;45:35208–22. https://doi.org/10.1016/j.ijhydene.2020.05.233.
[43] Bazooyar B, Darabkhani HG. Design and numerical analysis of a 3 kWe flameless microturbine combustor for hydrogen fuel. Int J Hydrogen Energy 2019;44:11134–44. https://doi.org/10.1016/j.ijhydene.2019.02.132.
[44] Fortunato V, Mosca G, Lupant D, Parente A. Validation of a reduced NO formation mechanism on a flameless furnace fed with H2-enriched low calorific value fuels. Appl Therm Eng 2018;144:877–89. https://doi.org/10.1016/j.applthermaleng.2018.08.091.
[45] Huang M, Deng H, Liu Y, Zhang B, Cheng S, Zhang X, et al. Effect of fuel type on the MILD combustion of syngas. Fuel 2020;281:118509. https://doi.org/10.1016/j.fuel.2020.118509.
[46] Chinnici A, Nathan GJ, Dally BB. Experimental and numerical study of the influence of syngas composition on the performance and stability of a laboratory-scale MILD combustor. Exp Therm Fluid Sci 2020;115:110083. https://doi.org/10.1016/j.expthermflusci.2020.110083.
[47] Shabanian SR, Derudi M, Rahimi M, Frassoldati A, Cuoci A, Faravelli T. Experimental and numerical analysis of syngas mild combustion. XXXIV Meet. Italy: Ital. Sect. Combust. Institute; 2011.
[48] Huang MM, Shao WW, Xiong Y, Liu Y, Zhang ZD, Lei FL, et al. Effect of fuel injection velocity on MILD combustion of syngas in axially-staged combustor. Appl Therm Eng 2014;66:485–92. https://doi.org/10.1016/j.applthermaleng.2014.02.033.
[49] Huang M, Zhang Z, Shao W, Xiong Y, Liu Y, Lei F, et al. Coal-derived syngas MILD combustion in parallel jet forward flow combustor. Appl Therm Eng 2014;71:161–8. https://doi.org/10.1016/j.applthermaleng.2014.06.044.
[50] Huang M, Zhang Z, Shao W, Xiong Y, Liu Y, Lei F, et al. Effect of air preheat temperature on the MILD combustion of syngas. Energy Convers Manag 2014;86:356–64. https://doi.org/10.1016/J.ENCONMAN.2014.05.038.
[51] Huang M, Xiao Y, Zhang Z, Shao W, Xiong Y, Liu Y, et al. Effect of air/fuel nozzle arrangement on the MILD combustion of syngas. Appl Therm Eng 2015;87:200–8. https://doi.org/10.1016/j.applthermaleng.2015.04.076.
[52] Amaduzzi R, Ferrarotti M, Parente A. Strategies for hydrogen-enriched methane flameless combustion in a quasi-industrial furnace. Front Energy Res 2021;8:353.
[53] Chinnici A, Nathan GJ, Dally BB. Experimental demonstration of the hybrid solar receiver combustor. Appl Energy 2018;224:426–37. https://doi.org/10.1016/j.apenergy.2018.05.021.
[54] Colorado AF, Herrera BA, Amell AA. Performance of a Flameless combustion furnace using biogas and natural gas. Bioresour Technol 2010;101:2443–9. https://doi.org/10.1016/j.biortech.2009.11.003.
[55] Sánchez M, Cadavid F, Amell A. Experimental evaluation of a 20kW oxygen enhanced self-regenerative burner operated in flameless combustion mode. Appl Energy 2013;111:240–6. https://doi.org/10.1016/j.apenergy.2013.05.009.
[56] Cano Ardila FE, Obando Arbeláez JE, Amell Arrieta AA. Emissions and dynamic stability of the flameless combustion regime using hydrogen blends with natural gas. Int J Hydrogen Energy 2021;46:1246–58. https://doi.org/10.1016/j.ijhydene.2020.09.236.
[57] Brohez S, Delvosalle C, Marlair G. A two-thermocouples probe for radiation corrections of measured temperatures in compartment fires. Fire Saf J 2004;39:399–411. https://doi.org/10.1016/j.firesaf.2004.03.002.
[58] Blevins LG, Pitts WM. Modeling of bare and aspirated thermocouples in compartment fires. Fire Saf J 1999;33:239–59. https://doi.org/10.1016/S0379-

7112(99)00034-X.
[59] Wabel TM, Zhang P, Zhao X, Wang H, Hawkes E, Steinberg AM. Assessment of chemical scalars for heat release rate measurement in highly turbulent premixed combustion including experimental factors. Combust Flame 2018;194:485–506. https://doi.org/10.1016/j.combustflame.2018.04.016.
[60] Si J, Wang G, Mi J. Characterization of MILD combustion of a premixed CH4/air jet flame versus its conventional counterpart. ACS Omega 2019;4:22373–84. https://doi.org/10.1021/acsomega.9b02711.
[61] Klein-Douwel RJH, Luque J, Jeffries JB, Smith GP, Crosley DR. Laser-induced fluorescence of formaldehyde hot bands in flames. Appl Opt 2000;39:3712–5. https://doi.org/10.1364/AO.39.003712.
[62] Gaydon A. The spectroscopy of flames. Springer Netherlands; 1974.
[63] Arias L, Torres S, Sbarbaro D, Farias O. Photodiode-based sensor for flame sensing and combustion-process monitoring. Appl Opt 2008;47:5541–9. https://doi.org/10.1364/AO.47.005541.
[64] Cui L, Li X, Yang G. Coupling Analysis of Chemiluminescence and Pressure Changes in CH 4/Air Explosion Suppressed by NaHCO 3 Powder 2020. https://doi.org/10.1021/acsomega.0c02834.
[65] Lupant D, Lybaert P. Assessment of the EDC combustion model in MILD conditions with in-furnace experimental data. Appl Therm Eng 2015;75:93–102. https://doi.org/10.1016/j.applthermaleng.2014.10.027.
[66] Li P, Mi J, Dally BB, Craig RA, Wang F. Premixed moderate or intense low-oxygen dilution (MILD) combustion from a single jet burner in a laboratory-scale furnace. Energy Fuel 2011;25:2782–93. https://doi.org/10.1021/ef200208d.
[67] Liao Y, Deng F, Xiao B. Hydrogen-rich gas production from catalytic gasification of pine sawdust over Fe-Ce/olivine catalyst. Int J Energy Res 2019;43:7486–95. https://doi.org/10.1002/er.4781.
[68] Richards G, Casleton K. Gasification technology to produce synthesis gas. Synth. Gas combust. CRC Press; 2009. p. 1–28. https://doi.org/10.1201/9781420085358.ch1.
[69] Casleton KH, Breault RW, Richards GA. System issues and tradeoffs associated with syngas production and combustion. Combust Sci Technol 2008;180:1013–52. https://doi.org/10.1080/00102200801962872.
[70] Bolhàr-Nordenkampf M, Rauch R, Bosch K, Aichernig C, Hofbauer H. Biomass CHP plant güssing – using gasification for power generation. In: Proceeding 2nd reg conf energy technol towar a clean environ 12-14 febr 2003, phuket thail; 2003. p. 566–72.
[71] Hofbauer H, Rauch R, Bosch K, Koch R, Aichernig C. Biomass CHP plant güssing - a success story. Expert Meet Pyrolysis Gasif Biomass Waste 2003:527–36.
[72] Rafidi N, Blasiak W. Thermal performance analysis on a two composite material honeycomb heat regenerators used for HiTAC burners. Appl Therm Eng 2005;25:2966–82. https://doi.org/10.1016/j.applthermaleng.2005.03.004.
[73] Rafidi N, Blasiak W. Heat transfer characteristics of HiTAC heating furnace using regenerative burners. Appl Therm Eng 2006;26:2027–34. https://doi.org/10.1016/j.applthermaleng.2005.12.016.
[74] Wang F, Mi J, Li P. Combustion regimes of a jet diffusion flame in hot co-flow. Energy Fuel 2013;27:3488–98. https://doi.org/10.1021/ef400500w.
[75] de Joannon M, Sorrentino G, Cavaliere A. MILD combustion in diffusion-controlled regimes of Hot Diluted Fuel. Combust Flame 2012;159:1832–9. https://doi.org/10.1016/j.combustflame.2012.01.013.
[76] Tu Y, Liu H, Chen S, Liu Z, Zhao H, Zheng C. Effects of furnace chamber shape on the MILD combustion of natural gas. Appl Therm Eng 2015;76:64–75. https://doi.org/10.1016/j.applthermaleng.2014.11.007.
[77] Li P, Wang F, Mi J, Dally BB, Mei Z. MILD combustion under different premixing patterns and characteristics of the reaction regime. Energy Fuel 2014;28:2211–26. https://doi.org/10.1021/ef402357t.
[78] Smith TF, Shen ZF, Friedman JN. Evaluation of coefficients for the weighted sum of gray gases model. J Heat Tran 1982;104:602–8. https://doi.org/10.1115/1.3245174.
[79] Wang L, Liu Z, Chen S, Zheng C. Comparison of different global combustion mechanisms under hot and diluted oxidation conditions. Combust Sci Technol 2012;184:259–76. https://doi.org/10.1080/00102202.2011.635612.
[80] Roache PJ. Perspective: a method for uniform reporting of grid refinement studies. J Fluid Eng 1994;116:405. https://doi.org/10.1115/1.2910291.
[81] Aminian J, Galletti C, Tognotti L. Extended EDC local extinction model accounting finite-rate chemistry for MILD combustion. Fuel 2016;165:123–33. https://doi.org/10.1016/J.FUEL.2015.10.041.
[82] Parente A, Malik MR, Contino F, Cuoci A, Dally BB. Extension of the Eddy Dissipation Concept for turbulence/chemistry interactions to MILD combustion. Fuel 2016;163:98–111. https://doi.org/10.1016/j.fuel.2015.09.020.
[83] Romero-Anton N, Huang X, Bao H, Martin-Eskudero K, Salazar-Herran E, Roekaerts D. New extended eddy dissipation concept model for flameless combustion in furnaces. Combust Flame 2020;220:49–62. https://doi.org/10.1016/J.COMBUSTFLAME.2020.06.025.
[84] Lezcano Benitez JC, Cadavid Sierra FJ. Numerical calculation of the recirculation factor in flameless furnaces. Fac Ing 2012:105. Tesis de m.
[85] Lezcano C, Obando J, Amell A. Numerical simulation of a flameless combustion furnace with mixtures of methane and a sub-bituminous pulverized Coal. Combust Sci Technol 2017;189:1591–604. https://doi.org/10.1080/00102202.2017.1305370.
[86] Wang F, Li P, Mei Z, Zhang J, Mi J. Combustion of CH4/O2/N2 in a well stirred reactor. Energy 2014;72:242–53. https://doi.org/10.1016/j.energy.2014.05.029.
[87] Luan C, Xu S, Shi B, Tu Y, Liu H, Li P, et al. Re-recognition of the MILD combustion regime by initial conditions of tin and XO2 for methane in a nonadiabatic well-stirred reactor. Energy Fuel 2020;34:2391–404. https://doi.org/10.1021/acs.energyfuels.9b04177.
[88] Smith GP, Golden DM, Frenklach M, Moriarty NW, Eiteneer B, Goldenberg M, et al. GRI-Mech 3.0. 2000.
[89] Yepes HA, Vargas AC, Arrieta AA. Kinetic study of the effect of sub-atmospheric conditions on the laminar burning velocity of high C2H6 content natural gas mixtures. Combust Theor Model 2022:1–27. https://doi.org/10.1080/13647830.2021.2016981.
[90] Sabia P, de Joannon M. Critical issues of chemical kinetics in MILD combustion. Front Mech Eng 2020;6:7.
[91] Yang Z, Li X, Wang Z, Wang Z. Assessment of chemical mechanism and chemical reaction sensitivity analysis for CH4/H2 flame under mild combustion environment. Therm Sci 2020;24:2101–11.